Numerical investigation of a novel smoldering-driven reactor for plastic waste pyrolysis

Ruming Pan, Gerald Debenest

Version of Record: https://www.sciencedirect.com/science/article/pii/S0196890422002357
Manuscript_298dad64f457ebece3ecf213a50780c7

Numerical investigation of a novel smoldering-driven reactor for plastic waste pyrolysis

Ruming Pan [a,*], Gérald Debenest [a]

[a] Institut de Mécanique des Fluides de Toulouse (IMFT) - Université de Toulouse, CNRS-INPT-UPS, Toulouse 31400, France

Corresponding Author *E-mails: ruming.pan@toulouse-inp.fr

Abstract

This study proposed a novel smoldering-driven reactor for plastic waste (PW) pyrolysis. The heat from self-sustaining smoldering was used to pyrolyze PW to produce oil and gas, a sustainable waste-to-energy approach. A multidimensional numerical model was developed to verify the feasibility and evaluate the performance of the proposed reactor. It was the first attempt to study the smoldering-driven pyrolysis of PW, including the melting process. The findings revealed that char smoldering could provide a stable propagating heat source for PW pyrolysis. The char concentration and air inlet velocity in the smoldering chamber could regulate the PW pyrolysis duration and product yields by controlling the peak temperature and heat propagation velocity. The pyrolysis product yields were controlled by PW content due to the change of velocity field in the pyrolysis chamber. The energy efficiency of PW pyrolysis was also evaluated under critical parameters.

Keywords

Plastic waste; Waste-to-energy; Smoldering; Pyrolysis; Multidimensional simulation

Nomenclature

Latin letters	
A	Pre-exponential factor, 1/s
A_s	Surface area, m^2
C	Concentration, %
C_p	Specific heat capacity, J/kg/K
d_p	Particle diameter, mm
D	Diffusion coefficient, m^2/s
E	Activation energy, kJ/mol
E_c	Consumed energy, kJ
E_{in}	Input energy, kJ
e_E	Energy efficiency, %
g_a	Gravitational acceleration, m/s^2
h_{cv}	Boundary gas convective heat transfer coefficient, $W/m^2/K$
h_{sg}	Interfacial heat transfer coefficient, $W/m^2/K$
k	Thermal conductivity, W/m/K
m	Mass, kg
M	Molecular weight, g/mol
n	Exponent
Nu	Nusselt number
p	Pressure, Pa
Pr	Prandtl number
q	Heat flux, W/m^2
r	Chamber radius, m
R	Reaction rate of char smoldering, 1/s
r_c	Radius of fixed bed particle, m
Re	Reynolds number
R_g	Ideal gas constant, J/mol/K
t	Time (duration), s
T	Temperature, ºC
u	Velocity, m/s
U	Boundary solid heat transfer coefficient, W/m/K
v	Stoichiometric coefficient
Y	Mass fraction
Greek symbols	
α_m	Phase transition, -
ΔH	Enthalpy of reaction, MJ/kg

ΔT	Melting transition zone length, K
ε_p	Porosity
θ	Solid phase fraction
κ_p	Permeability, m^2
μ	Dynamic viscosity, $Pa \cdot s$
ρ	Density, kg/m^3
σ	Stefan–Boltzmann constant, $W/m^2/K^4$
Subscripts/superscript	
app	Apparent
bed	Bed material in pyrolysis chamber
eff	Effective
f	Fluid in pyrolysis chamber
g	Gases in smoldering chamber
G	Pyrolysis gas
in	Inlet
L	PW pyrolysis liquid
L+	Heavy fraction in pyrolysis liquid
L-	Light fraction in pyrolysis liquid
mPW	Melted plastic waste
0	Initial
O_2	Oxygen
p	Peak value
pc	Phase change
ph	Phase
PW	Plastic waste
py	Pyrolysis
rad	Radiation
Res	PW pyrolysis residue
s	Solid in smoldering chamber
smo	Smoldering
sp	Sphere
sPW	Solid plastic waste
∞	Ambient

1. Introduction

Smoldering, a flameless type of combustion, is an emerging solution to many environmental and energy challenges [1]. Smoldering takes place in a porous medium, allowing air to diffuse and react with the reactants. Smoldering can be a self-sustaining

process when the heat retained and released by the oxidation of the reactants exceeds the heat loss [2].

Self-sustaining smoldering is a promising method to treat contaminated soils, dispose of wastes, and realize waste valorization [3]. The organic contaminants, e.g., bitumen [4], coal tar [5], and wastewater sludge [6], can be destroyed by oxidation to clean the soil. Wastes, such as feces [7], waste tires [8], and food waste [9], can also be disposed of by smoldering. There are two modes of waste valorization using the heat from smoldering, i.e., in-situ [9-11] and ex-situ [12-13]. The in-situ scenario represents that smoldering and waste valorization occur in the same chamber, allowing the heat and mass transfer between the two reactions. In the ex-situ scenario, smoldering and waste valorization occur in two chambers, and only the heat from smoldering is transported through the boundary for waste valorization.

Self-sustaining smoldering contains a reaction front, where the reactants react with oxygen in the air. The heat released by smoldering accumulates in the porous medium and forms a heatwave [14]. It is noteworthy that the velocities of the reaction front and heat front may be different. In practical application scenarios of smoldering-driven waste valorization, temperature and heat propagation velocity are two vital factors, which can determine the product distribution and process duration. Duque et al. [13], Bittencourt et al. [15], and Ronda et al. [16] confirmed that higher temperatures and faster heat propagation velocities could shorten the duration of waste disposal. Feng et al. [17] suggested that sewage sludge was destructed faster to produce value-added fuels at a higher temperature. Moreover, smoldering reactant concentration and air velocity are the two most important factors controlling

temperature and heat propagation velocity [4,18].

Oxidation of reactants during smoldering may change the volume and porosity of porous media, which leads to fluctuations in temperature and propagation velocity. Duque et al. [12-13] reported that the peak temperature during char smoldering fluctuated in a wide range of 400–800ºC. Moreover, a high peak-temperature difference of ~300ºC and bed shrinkage were observed during granular activated charcoal smoldering [19]. The fluctuations are not conducive to the utilization of smoldering heat. Mixing reactants with sand effectively addresses the smoldering propagation instability that occurs during reactant-only smoldering [2]. High heat capacity sand maintains the bed volume and porosity and regulates the temperature, resulting in a nearly constant peak temperature and front velocity [20]. The self-sustaining smoldering with a stable propagation velocity and temperature makes it favorable for pyrolysis applications.

On the other hand, plastics are widely used due to their superior properties. However, there is a considerable accumulation of plastic waste (PW) in the environment due to the improper handling of plastics [21]. Pyrolysis, thermal decomposition in an inert atmosphere, is a promising way to convert plastic waste (PW) into value-added products (liquid and gaseous fuels) [22]. PW pyrolysis will undergo three processes, i.e., heating, melting, and decomposing [23]. It is challenging to heat PW uniformly due to its low thermal conductivity [24], which hinders the application of PW pyrolysis at the reactor scale [25]. Mixing PW with high-thermal-conductivity solid particles for heating may be a promising way to improve the heat transfer performance in the reactor [26-27].

Based on the above discussion, this study proposes a novel smoldering-driven reactor for the pyrolysis of PW. The reactor consists of two chambers: (i) the smoldering chamber is filled with char and sand, and (ii) the pyrolysis chamber is filled with PW and high-thermal-conductivity bed material. A one-dimensional (1D) smoldering model is coupled with a two-dimensional (2D) pyrolysis model to investigate the smoldering-driven pyrolysis of PW. To the best of our knowledge, it is the first investigation of the smoldering-driven pyrolysis of PW, which includes the melting process. The 1D smoldering model and 2D pyrolysis model are validated based on the previous experimental results. Then, the validated multidimensional model is utilized to study the PW pyrolysis duration, product yields, and energy efficiency under different operating conditions (char concentration, air inlet velocity, and PW content).

2. Methods

2.1.Reactor description

Fig. 1 demonstrates the schematic of the smoldering-driven reactor for PW pyrolysis. The reactor has two separate chambers: the outer one is the smoldering chamber, and the inner one is the pyrolysis chamber. The smoldering chamber is filled with a mixture of sand and char. The top of the smoldering chamber is equipped with a heating device for the char ignition. After the heating device heats the smoldering chamber 1020s, the air is pumped into the chamber by an air pump. The heating device is turned off after 4320s, while the air supply remains unchanged. The char spontaneously smoldering propagates downward, and the gases

produced by the smoldering flow out through the bottom outlet. The smoldering heat is introduced into the pyrolysis chamber through the inner boundary of the smoldering chamber.

The pyrolysis chamber is a fixed bed with a porous structure. PW pellets fill the empty volume within the chamber. The thermal conductivity of PW is very low (0.42–0.45W/m/K) [23]. The porous matrix is a high thermal conductivity material, which allows for a more uniform radial temperature distribution (compared to PW pyrolysis alone) in the chamber [26]. As the temperature inside the chamber increases, PW is first melted and then pyrolyzed into volatiles, increasing the chamber's porosity from 0 to that of the fixed bed. It is noteworthy that the volatile products can spontaneously flow out from the top of the chamber due to the pressure difference generated during the pyrolysis of PW.

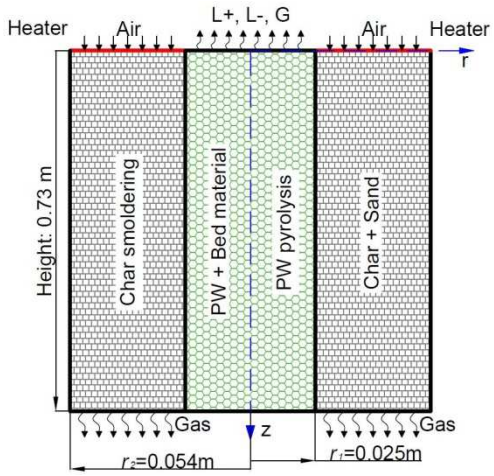

Fig. 1. Illustration of the smoldering-driven reactor for PW pyrolysis.

Table 1 shows the numerical model input parameters.

Table 1. Numerical model input parameters.

Case	Char concentration (%)	Air inlet velocity (m/s)	PW content (-)
1 [a-b]	2.0	0.030	0.40
2 [b]	2.1	0.030	0.40

3 [b]	2.2	0.030	0.40
4 [b]	2.3	0.030	0.40
5 [b]	2.4	0.030	0.40
6 [b-d]	2.5	0.030	0.40
7 [c]	2.5	0.035	0.40
8 [c]	2.5	0.040	0.40
9 [c]	2.5	0.045	0.40
10 [c]	2.5	0.050	0.40
11 [d]	2.5	0.030	0.30
12 [d]	2.5	0.030	0.35
13 [d]	2.5	0.030	0.45
14 [d]	2.5	0.030	0.50

[a] Base case.

[b] Study on the effect of char concentration.

[c] Study on the effect of air inlet velocity.

[d] Study on the effect of PW content.

2.2.Reaction kinetics

Char smoldering consumes oxygen to produce gases and releases large amounts of heat [2,20,28-29]:

$$Char + v_{O_2} O_2 \xrightarrow{R_{Char}} gases \quad (1)$$

$$R_{Char} = A_{Char} \exp(-E_{Char}/(R_g T_s)) Y_{Char}^{n_{Char}} Y_{O_2}^{n_{O_2}} \quad (2)$$

Fig. 2 demonstrates the lumped pyrolysis pathways of plastic waste (PW). As the temperature rises, PW is first melted and then decomposed [23]. This study adopts the assumption of one-step primary cracking and two-step secondary cracking. The melted PW is decomposed into heavy (L+, C5–C15) and light (L-, >C15) liquids, gas (G, C1-C4), and residue (C) [30-31]. The primary cracking is considered a one-step process [23,32-33]. It is noteworthy that PW is waste polyethylene recycled from municipal solid waste in the present study [34]. The residue yield remained almost unchanged (3.4–4.0wt%) under different

operating conditions when PW was fully pyrolyzed [34]. Therefore, the residue is considered to form only during the primary cracking. Since the pyrolysis takes place in a non-purging atmosphere, the residence time of the pyrolysis volatiles in the pyrolysis chamber is relatively long. The secondary cracking reactions must be considered [30].

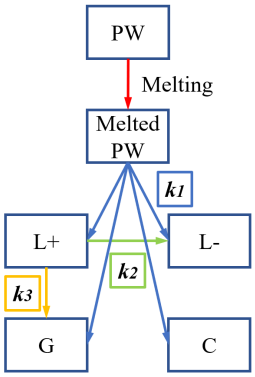

Fig. 2. Lumped pyrolysis pathways of PW.

The reaction mechanism and reaction rates of PW pyrolysis follow:

$$PW \xrightarrow{R_{PW}} v_L((v_{L+}L+) + (v_{L-}L-)) + v_G G + v_{Res}Residue \tag{3}$$

$$L+ \xrightarrow{R_{L+:L-}} L- \tag{4}$$

$$L+ \xrightarrow{R_{L+:G}} G \tag{5}$$

$$R_{PW} = A_{PW}\exp(-E_{PW}/(R_g T_{PW}))\rho_{PW} \tag{6}$$

$$R_{L+:L-} = A_{L-}\exp(-E_{L-}/(R_g T_{PW}))\rho_{L+} \tag{7}$$

$$R_{L+:G} = A_G\exp(-E_G/(R_g T_{PW}))\rho_{L+} \tag{8}$$

Accordingly, the reaction rates of L+ (R_{L+}), L- (R_{L-}), and G (R_G) are:

$$R_{L+} = v_L v_{L+} R_{PW} - R_{L+:L-} - R_{L+:G} \tag{9}$$

$$R_{L-} = v_L v_{L-} R_{PW} + R_{L+:L-} \tag{10}$$

$$R_G = v_G R_{PW} + R_{L+:G} \tag{11}$$

The L+ yield (Y_{L+}), L- yield (Y_{L-}), and G yield (Y_G) are determined by:

$$Y_{L+} = m_{L+}/m_{PW,0} \quad (12)$$

$$Y_{L-} = m_{L-}/m_{PW,0} \quad (13)$$

$$Y_G = m_G/m_{PW,0} \quad (14)$$

Table 2 lists the kinetic parameters of char smoldering and PW pyrolysis.

Table 2. Kinetic parameters of char smoldering and PW pyrolysis.

Par.	Value	Unit	Ref.
A_{Char}	707.9	s^{-1}	[20]
E_{Char}	68	kJ/mol	[20]
ΔH_{Char}	-30.82×10^{3}	kJ/kg	[20]
A_{PW}	1.12×10^{22}	s^{-1}	Calibrated
E_{PW}	346.8	kJ/mol	[32]
ΔH_{PW}	323	kJ/kg	[23]
A_{L-}	9.49×10^{-3}	s^{-1}	[30]
E_{L-}	0.372	kJ/mol	[30]
ΔH_{L-}	-42	kJ/kg	[26]
A_G	8.10×10^{-1}	s^{-1}	[30]
E_G	18.2	kJ/mol	[30]
ΔH_G	-42	kJ/kg	[26]
n_{Char}	1	-	[20]
n_{O2}	1	-	[20]
v_{O2}	1.15	-	[20]
v_L	0.8350	-	[34]
v_G	0.1285	-	[34]
v_{Res}	0.0365	-	[34]
v_{L+}	0.863	-	[34]
v_{L-}	0.137	-	[34]
R_g	8.314	J/mol/K	[35]

2.3.Governing equations

The char smoldering was developed as a one-dimensional (1D) model (Section 2.3.1), while the PW pyrolysis was developed as a two-dimensional (2D) model (Section 2.3.2). There is only heat transfer (no mass transfer) between the smoldering and pyrolysis chambers,

which exchanges through the boundary. The governing equations of developed models were solved in COMSOL.

2.3.1. Char smoldering

The char and air conservations are calculated by:

$$\frac{\partial}{\partial t}(Y_{Char}) = -R_{Char} \tag{15}$$

$$\frac{\partial}{\partial t}(\varepsilon_{p,smo}\rho_g) + \nabla \cdot (\rho_g u_g) = \rho_{Char} R_{Char} \tag{16}$$

where the porosity of smoldering bed is $\varepsilon_{p,smo} = \varepsilon_{p,smo,0}(1 - Y_{Char}C_{Char})$, and the air velocity u_g obeys Darcy's Law:

$$u_g = -(\kappa_{p,smo}/\mu_g)\nabla p_g \tag{17}$$

The oxygen transport equation follows:

$$\frac{\partial}{\partial t}(\varepsilon_{p,smo}\rho_g Y_{O_2}) + \nabla \cdot (\rho_g u_g Y_{O_2}) = \nabla \cdot (\varepsilon_{p,smo}\rho_g D_g \nabla Y_{O_2}) - \rho_{Char} v_{O_2} R_{Char} \tag{18}$$

The heat transport equations for solid (T_s) and air (T_g) are defined by Eq. (19) and Eq. (20) as follows:

$$\frac{\partial(\rho C_p)_{eff,smo} T_s}{\partial t} = \nabla \cdot \left(k_{eff,smo} \nabla T_s\right) + h_{sg}(A_{s,sp}/V_{sp})(T_g - T_s) - \rho_{Char} \Delta H_{Char} R_{Char} \tag{19}$$

$$\frac{\partial \varepsilon_{p,smo}(\rho_g C_{p,g}) T_g}{\partial t} + \nabla \rho_g C_{p,g} u_g T_g = \nabla \cdot \left(\varepsilon_{p,smo} k_g \nabla T_g\right) + h_{sg}(A_{s,sp}/V_{sp})(T_s - T_g) \tag{20}$$

where the interfacial heat transfer coefficient h_{sg} is calculated by $Nu = h_{sg} d_{p,Sand}/k_g = 0.001(Re^{1.97} Pr^{1/3})$ [36], the surficial area per unit volume $A_{s,sp}/V_{sp} = 6(1 - \varepsilon_{p,smo})/d_{p,Sand}$ [20], and the solid (sand and char) effective properties of $(\rho C_p)_{eff,smo}$ and $k_{eff,smo}$ are described by:

$$(\rho C_p)_{eff,smo} = \left(1 - \varepsilon_{p,smo,0}\right)\rho_{Sand} C_{p,Sand} + Y_{Char}\rho_{Char} C_{p,Char} \tag{21}$$

$$k_{eff,smo} = \left(1 - \varepsilon_{p,smo,0}\right)\left(k_{Sand} + k_{rad}\right) + Y_{Char} C_{Char} \varepsilon_{p,smo,0} k_{Char} \quad (22)$$

where the radiation heat transfer is calculated by Rosseland approximation ($k_{rad} = 16\sigma d_{p,Sand} {T_s}^3/3$) [37].

The initial and boundary conditions, and the parameters of smoldering model are tabulated in Tables 3 and 4, respectively.

Table 3. Initial and boundary conditions of smoldering model.

Initial Condition	Boundary Condition
t=0s: $Y_{Char} = 1$	-
t=0s: $p_g = 101375\text{Pa}$	z=0.000m: $\begin{cases} t = (0,1020s): u_g = 0 \\ t = (1020s, 30000s): u_g = u_{g,in} \end{cases}$
	z=0.730m: $p_g = 101375\text{Pa}$
t=0s: $Y_{O_2} = 0.204$	z=0.000m: $Y_{O_2} = 0.204$
	z=0.730m: $-\varepsilon_{p,smo} D_g \nabla \cdot (\rho_g Y_{O_2}) = \rho_g u_g (Y_{O_2,0} - Y_{O_2})$
t=0s: $T_s = 293.15\text{K}$	z=0.000m: $\begin{cases} t = (0,4320s): -k_{eff,smo} \nabla T_s = 25\text{kW/m}^2 \\ t = (4320s, 30000s): -k_{eff,smo} \nabla T_s = 0 \end{cases}$
	z=0.730m: $-k_{eff,smo} \nabla T_s = 0$
t=0s: $T_g = 293.15\text{K}$	z=0.000m: $T_g = 293.15\text{K}$
	z=0.730m: $-k_g \nabla T_g = 0$
-	z axis: $-k_{eff,smo} \nabla T_s = U\left[\frac{2}{r_{smo}}(T_s - T_\infty) + \frac{2}{r_{py}}(T_s - T_{PW})\right]$
-	z axis: $-k_g \nabla T_g = h_{cv}(T_g - T_{PW})$

Table 4. Model inputs and materials' physical parameters of smoldering model.

Par.	Value	Unit	Ref.
r_{smo}	0.054	m	[20]
$d_{p,Sand}$	0.88	mm	[20]
D_g	4.53×10^{-5}	m^2/s	[20]
μ_g	$-9\times10^{-12}(T_g^2)+4\times10^{-8}(T_g)+6\times10^{-6}$	Pa·s	[36]
k_{Char}	0.25	W/m/K	[20]
k_{Sand}	$0.000541(T_s)+0.1044$	W/m/K	[36]
k_g	$-1\times10^{-8}(T_g^2)+8\times10^{-5}(T_g)+4.3\times10^{-3}$	W/m/K	[36]
m_{Char}	0.207	kg	[20]
m_{Sand}	10.34	kg	[20]
C_{Char}	m_{Char}/m_{Sand}=2.0	%	Calibrated

ρ_{Char}	31.80	kg/m^3	[20]
ρ_{Sand}	2650	kg/m^3	[20]
$C_{p,Char}$	1100	J/kg/K	[20]
$C_{p,Sand}$	2.49(T_s)+39.06	J/kg/K	[36]
$C_{p,g}$	-3×10^{-5}(T_g^2)+0.2261 (T_g)+940.35	J/kg/K	[36]
$\kappa_{p.smo}$	2.54×10^{-10}	m^2	[20]
M_g	28.97	g/mol	[20]
$\varepsilon_{p,smo,0}$	0.4	-	[20]
σ	5.67×10^{-8}	W/m^2/K^4	[37]
U	5	W/m/K	[20]
h_{cv}	3.0645(u_g)+4.1115	W/m^2/K	[38]
q_{in}	25000	W/m^2	[36]
$u_{g,in}$	0.05	m/s	[20]
T_∞	293.15	K	This study

2.3.2. PW pyrolysis

(1) Melting

The modified apparent heat capacity method (AHCM) is used to simulate the melting process of PW [23]. The modified AHCM adopts a Heaviside step function of $\theta(T_{PW})$ (Fig. A.1) to indicate the phase transitions in PW. The energy conservation equation follows:

$$(\rho C_p)_{eff,melt}\frac{\partial T_{PW}}{\partial t} = \nabla \cdot \left(k_{eff,melt}\nabla T_{PW}\right) \tag{23}$$

It is noteworthy that the melted PW is considered to be a stationary fluid due to the high viscosity (>10^{3}Pa·s) at low share rates [23,39-40]. The effective volumetric heat capacity $(\rho C_p)_{eff,melt}$ and the effective thermal conductivity $k_{eff,melt}$ follow:

$$(\rho C_p)_{eff,melt} = \left(1-\varepsilon_{p,bed}\right)\rho_{bed}C_{p,bed} + \varepsilon_{p,bed}\rho_{PW,eff}C_{p,app} \tag{24}$$

$$k_{eff,melt} = \left(1-\varepsilon_{p,bed}\right)k_{bed} + \varepsilon_{p,bed}k_{PW,eff} \tag{25}$$

where the PW effective density $\rho_{PW,eff}$, the PW effective thermal conductively $k_{PW,eff}$, and the PW apparent heat capacity $C_{p,app}$ are defined by:

$$\rho_{PW,eff} = \theta(T_{PW})\rho_{sPW} + (1 - \theta(T_{PW}))\rho_{mPW} \quad (26)$$

$$k_{PW,eff} = \theta(T_{PW})k_{sPW} + (1 - \theta(T_{PW}))k_{mPW} \quad (27)$$

$$C_{p,app} = \frac{1}{\rho_{PW,eff}}\left(\theta(T_{PW})\rho_{sPW}C_{p,sPW} + \left(1 - \theta(T_{PW})\right)\rho_{mPW}C_{p,mPW}\right) + \Delta H_{pc}\frac{d\alpha_m}{dT_{PW}} \quad (28)$$

where $\theta(T_{PW})$ represents the solid phase fraction, $1 - \theta(T_{PW})$ represents the molten phase fraction, and the phase transition between solid phase and molten phase $\alpha_m = -\frac{1}{2}\frac{\theta(T)\rho_{sPW} - (1-\theta(T))\rho_{mPW}}{\theta(T)\rho_{sPW} + (1-\theta(T))\rho_{mPW}}$.

(2) Decomposition

The melted PW (mPW) and fluid (L+, L-, and G) conservations are determined by:

$$\frac{\partial}{\partial t}(\rho_{mPW}) = -R_{PW} \quad (29)$$

$$\frac{\partial}{\partial t}\left(\varepsilon_{p,py}\rho_f\right) + \nabla \cdot \left(\rho_f \mathbf{u}\right) = R_{L+} + R_{L-} + R_G \quad (30)$$

where the fluid density ρ_f obeys the idea gas law, the porosity of PW fixed bed in a pyrolysis chamber is $\varepsilon_{p,py} = \varepsilon_{p,bed} - \left(\varepsilon_{p,bed} - \varepsilon_{p,py,0}\right)\rho_{mPW}/\rho_{PW,0}$, and the fluid velocity $\mathbf{u}$ obeys Darcy's Law (including gravity):

$$\mathbf{u} = -\frac{\kappa_{p,py}}{\mu_f}(\nabla p_f - \rho_f \boldsymbol{g_a}) \quad (31)$$

where the permeability of PW fixed bed in a pyrolysis chamber is determined by $\kappa_{p,py} = r_c^2\varepsilon_{p,py}^3/(180(1-\varepsilon_{p,py})^2)$ [29].

The L+, L-, and G transport equations follow:

$$\frac{\partial}{\partial t}\left(\varepsilon_{p,py}\rho_{L+}\right) + \nabla \cdot (\rho_{L+}\mathbf{u}) = \nabla \cdot \left(\varepsilon_{p,py}D_{L+}\nabla\rho_{L+}\right) + R_{L+} \quad (32)$$

$$\frac{\partial}{\partial t}\left(\varepsilon_{p,py}\rho_{L-}\right) + \nabla \cdot (\rho_{L-}\mathbf{u}) = \nabla \cdot \left(\varepsilon_{p,py}D_{L-}\nabla\rho_{L-}\right) + R_{L-} \quad (33)$$

$$\frac{\partial}{\partial t}\left(\varepsilon_{p,py}\rho_G\right) + \nabla \cdot (\rho_G\mathbf{u}) = \nabla \cdot \left(\varepsilon_{p,py}D_G\nabla\rho_G\right) + R_G \quad (34)$$

The energy conservation equation is calculated by:

$$\frac{\partial(\rho C_p)_{eff,py}T_{PW}}{\partial t} + \nabla\cdot((\rho C_p)_{eff,py}\mathbf{u}T_{PW}) = \nabla\cdot\left(k_{eff,py}\nabla T_{PW}\right) - R_{PW}\Delta H_{PW} - R_{L+:L-}\Delta H_{L-} - \\ -R_{L+:G}\Delta H_G \quad (35)$$

where the effective volumetric heat capacity $(\rho C_p)_{eff,py}$ and the effective thermal conductivity $k_{eff,py}$ are defined by:

$$(\rho C_p)_{eff,py} = \left(1-\varepsilon_{p,bed}\right)\rho_{bed}C_{p,bed} + \left(\varepsilon_{p,bed}-\varepsilon_{p,py}\right)\rho_{mPW}C_{p,mPW} + \varepsilon_{p,py}\rho_f C_{p,f} \quad (36)$$

$$k_{eff,py} = \left(1-\varepsilon_{p,bed}\right)k_{bed} + \left(\varepsilon_{p,bed}-\varepsilon_{p,py}\right)k_{mPW} + \varepsilon_{p,py}k_f \quad (37)$$

The initial and boundary conditions, and the parameters of pyrolysis model are listed in Tables 5 and 6, respectively.

Table 5. Initial and boundary conditions of pyrolysis model.

Initial Condition	Boundary Condition
t=0s: $\rho_{PW} = 380\text{kg/m}^3$	-
t=0s: $\rho_{L+} = 0\text{kg/m}^3$	r=0.000m&0.025m: $-\mathbf{n}\cdot(-D_{L+}\nabla\rho_{L+} + \mathbf{u}\rho_{L+}) = 0$
t=0s: $\rho_{L-} = 0\text{kg/m}^3$	r=0.000m&0.025m: $-\mathbf{n}\cdot(-D_{L-}\nabla\rho_{L-} + \mathbf{u}\rho_{L-}) = 0$
t=0s: $\rho_G = 0\text{kg/m}^3$	r=0.000m&0.025m: $-\mathbf{n}\cdot(-D_G\nabla\rho_G + \mathbf{u}\rho_G) = 0$
t=0s: $\varepsilon_{p,py} = 0$	-
t=0s: $\begin{cases}\mathbf{u} = 0\text{m/s}\\ p_f = 101375\text{Pa}\end{cases}$	z=0.000m: $p_f = 101375\text{Pa}$
	z=0.730m: $\mathbf{u} = 0\text{m/s}$
	r=0.000m: $\mathbf{u}\cdot\mathbf{n} = 0\text{m/s}$
	r=0.025m: $\mathbf{u} = 0\text{m/s}$
t=0s: $T_{PW} = 293.15\text{K}$	z=0.000m: $k_{eff,py}\nabla T_{PW} = 0$
	z=0.730m: $-\mathbf{n}\cdot\mathbf{q} = 0$
	r=0.000m: $k_{eff,py}\nabla T_{PW} = 0$
	r=0.025m: $k_{eff,py}\nabla T_{PW} = (1-\varepsilon_{p,smo})U\frac{2}{r_{py}}(T_s - T_{PW}) + \varepsilon_{p,smo}h_{cv}(T_g - T_{PW})$

Table 6. Model inputs and materials' physical parameters of pyrolysis model.

Par.	Value	Unit	Ref.
T_{pc}	138.5	℃	[23]

ΔT	32	℃	[23]
ΔH_{pc}	125	kJ/kg	[23]
ρ_{sPW}	950	kg/m^3	[41]
ρ_{mPW}	950	kg/m^3	[23]
k_{sPW}	0.42	W/m/K	[23]
k_{mPW}	0.45	W/m/K	[23]
$C_{p,sPW}$	1800	J/kg/K	[23]
$C_{p,mPW}$	2500	J/kg/K	[23]
r_{py}	0.025	m	This study
r_c	0.001	m	This study
D_0	5.6×10^{-5}	m^2/s	[42]
D_{L+}	$D_0(T_{PW}/273)^{1.7}$	m^2/s	[42]
D_{L-}	$D_0(T_{PW}/273)^{1.7}$	m^2/s	[42]
D_G	$D_0(T_{PW}/273)^{1.7}$	m^2/s	[42]
μ_f	3.0×10^{-5}	Pa·s	[26]
g_a	-9.8	m/s^2	[43]
k_f	0.02557	W/m/K	[26]
k_{bed}	10	W/m/K	[26]
$\varepsilon_{p,py,0}$	0	-	This study
$\varepsilon_{p,bed}$	0.4	-	This study
$\rho_{PW,0}$	$\rho_{sPW}(\varepsilon_{p,bed}-\varepsilon_{p,py,0})=380$	kg/m^3	Calibrated
ρ_{bed}	2650	kg/m^3	[26]
$C_{p,f}$	2356.3	J/kg/K	[24]
$C_{p,bed}$	800	J/kg/K	[26]
M_{L+}	331	g/mol	[34]
M_{L-}	166	g/mol	[34]
M_G	30	g/mol	[26]

This study adopts the energy efficiency (e_E) to evaluate the heat utilization of PW pyrolysis in the pyrolysis chamber. e_E is the proportion of energy consumed (E_c) in the input energy (E_{in}) [13]:

$$e_E = \frac{E_c}{E_a} \times 100\% \tag{38}$$

3. Results and discussion

3.1.Model verification

3.1.1. Char smoldering verification

Fig. 3 depicts the comparison between the experimental [20] and numerically calculated temperature profiles. The numerical calculation used Eqs. (15–22). Moreover, the initial and boundary conditions are listed in Tables 3 and 4. The calculated temperature drops faster than the experimental value during the cooling stage, which can be attributed to the overestimated speed of boundary heat loss. It can be seen that the smoldering could steadily propagate at an almost constant velocity and peak temperature. The numerically calculated average peak temperature and smoldering front velocity (635℃ and 3.24mm/min) are in good agreement with the experimental values (631℃ and 3.42mm/s), with errors equal to 0.6% and 5.3%, respectively. Moreover, Fig. A.3 reveals that the simulated pressure agrees well with the experimental data.

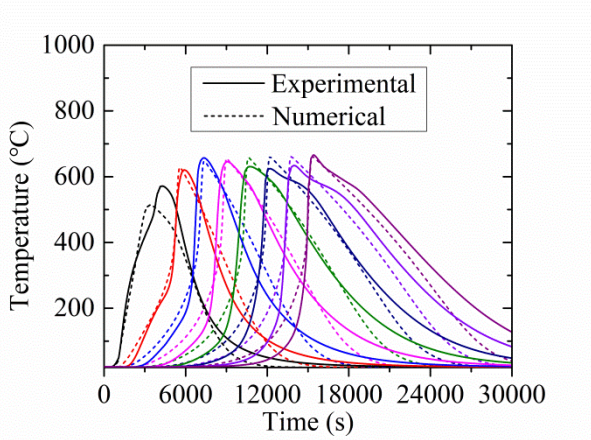

Fig. 3. Experimental and numerically calculated temperature profiles at z=0.04–0.67m with 0.09m intervals under C_{Char}=2.0% and $u_{g,in}$=0.05m/s.

3.1.2. PW pyrolysis verification

Fig. 4 demonstrates the experimental [23] and numerically calculated PW pyrolysis mass

fraction and heat flow. The experiment was conducted using a thermogravimetric analyzer coupled with a differential scanning calorimeter. The PW sample was heated from 25ºC to 500ºC at a heating rate of 8ºC/min. It should be noted that the pyrolysis volatiles (liquid and gas) were quickly taken away from the main reaction zone by the purge gas. Therefore, the liquid secondary cracking reactions were not taken into consideration. The numerical calculation used Eqs. (23–37). Fig. 4a shows that the simulated PW mass fraction agrees well with the experimental data, with an error of 1.1%. The heat flow curve has two peaks (Fig. 4b) in 122–154ºC and 430–500ºC, corresponding to the melting (solid phase to molten phase) and pyrolysis (molten phase to gas phase) processes. The negative heat flow indicates that the PW melting and pyrolysis are endothermic processes. The simulated peak temperatures of melting and pyrolysis are in good agreement with the experimental values, with errors equal to 0.6% and 17.9%, respectively.

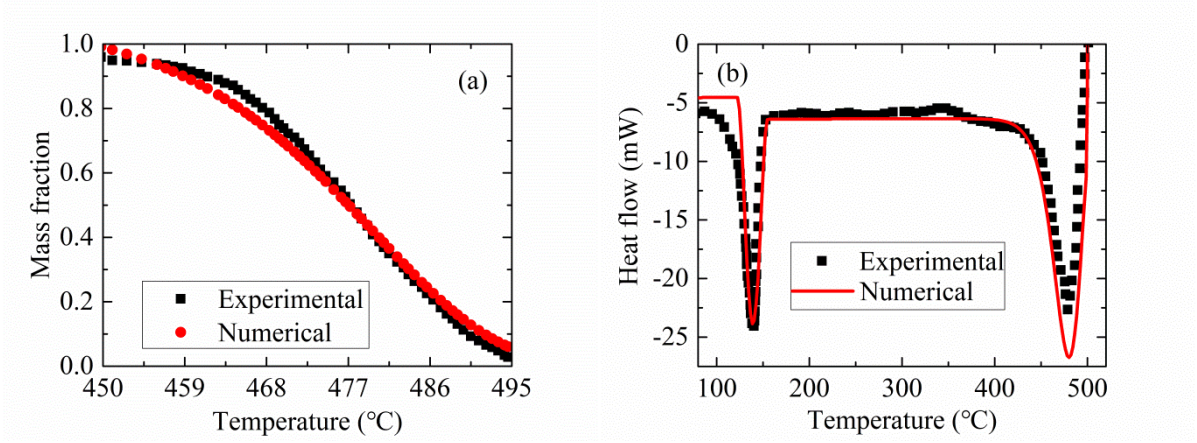

Fig. 4. Experimental and numerically calculated PW pyrolysis (a) mass fraction and (b) heat flow.

3.2.Process assessments

Fig. 5a shows T_S and T_{PW} longitudinal distributions at different times. The mesh of the

smoldering model is a line 0.73m long with 200 equally spaced nodes. Fig. A.4a shows the mesh size used for PW pyrolysis. The findings illustrated that the smoldering propagated stably at a front velocity of 2.25mm/min and a peak temperature of 620ºC. The average peak value of T_{PW} was 518ºC, which was approximately 100ºC lower than that of T_S. The lower T_{PW} was attributed to the heat loss in radial heat transfer and the heat consumed by PW melting and pyrolysis. The peak T_{PW} lagged behind the peak T_S by ~0.0605m due to the heat of smoldering accumulated behind the smoldering front [20]. Consequently, the peak T_{PW} increased from 508ºC at 7200s to 525ºC at 14400s due to the increasing accumulated heat.

On the other hand, the T_S peak was sharp, while the T_{PW} was round. Fig. 5b illustrates that the reaction zone in the smoldering chamber was very thin (~0.003m). The char reacted with oxygen to release intense heat, which provided a heat source with a high-power density and led to a rapid increase in local T_S (Fig. 5c). Note that the pyrolysis chamber was heated by the boundary heat flux from the smoldering chamber, so the relatively wide heating area (~0.1m) resulted in a round T_{PW} peak (Fig. 5d).

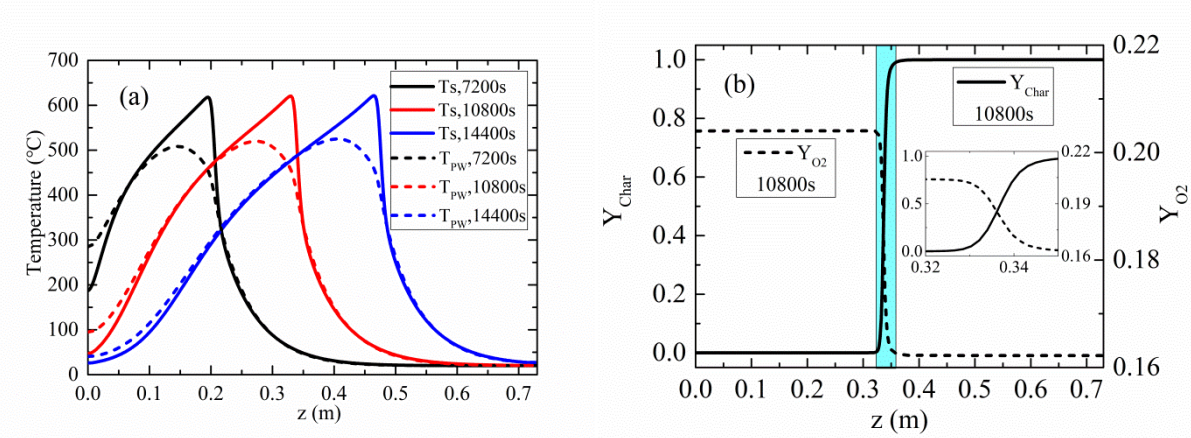

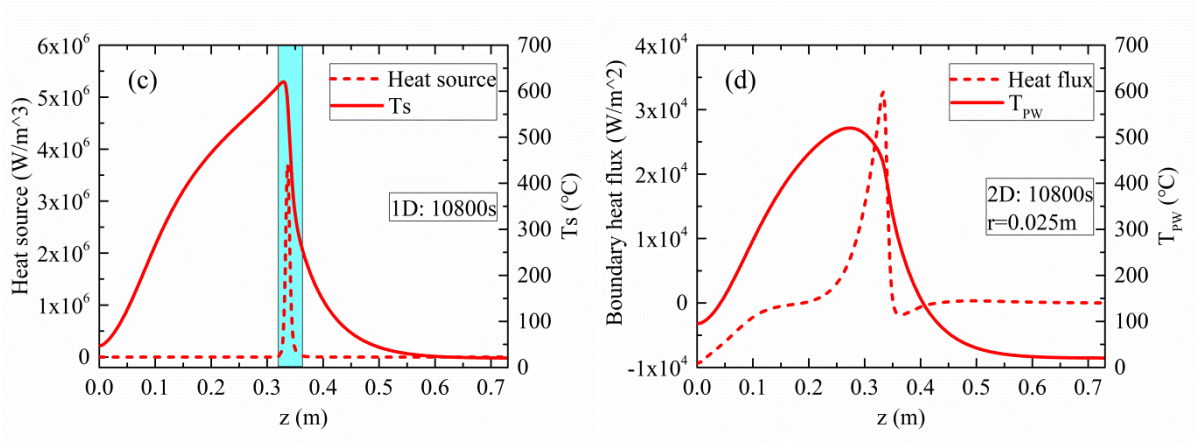

Fig. 5. Reactor thermal evaluation: (a) T_S and T_{PW} (at r=0.025m) profiles; (b) Y_{Char} and Y_{O2} profiles in smoldering chamber; (c) T_S and smoldering heat source; (d) T_{PW} and boundary heat flux.

Fig. 6a demonstrates that the temperature could propagate downward in the pyrolysis chamber. The increase in the high-temperature area indicated that the average T_{PW} increased with time, which was ascribed to the heat accumulation in the smoldering chamber [20]. Fig. 6b shows that the pyrolysis of PW took place within a layer of ~0.02m, and T_{PW} in this interval was 455–485℃, which was consistent with the results of the thermogravimetric experiment (Fig. 4). As depicted in Fig. 6c, the solid PW (dark region) was first melted at ~138℃, and then the melted PW (red region) was pyrolyzed into volatiles (blue region). The volatiles spontaneously flowed out from the top of the chamber due to the pressure difference generated during the pyrolysis of PW (Fig. A.4b). Consequently, the porosity increased from 0 to 0.4 when the melted PW was thoroughly decomposed (Fig. 6d). The permeability likewise increased from 0 to $9.88 \times 10^{-10} m^2$ due to the change in porosity (Fig. A.4c).

It should be noted that the PW pyrolysis was driven by the boundary heat flux from the smoldering chamber. Therefore, the change in T_{PW} was determined by T_S. Fig. 6e shows that,

except for Periods 1–2, L+ fraction decreased with time, while L- and G fractions increased with time, which could be ascribed to the increase in $T_{PW,p}$ (Fig. 5a) that exacerbated the secondary cracking of L+. Period 1 corresponded to the char ignition (t=2040s) in the smoldering chamber, which resulted in the smoldering propagation and PW pyrolysis. The pyrolysis of PW produced volatiles (L+, L-, and G), which caused the velocity in the pyrolysis chamber to increase from 0 to 0.03m/s. The increasing velocity shortened residence time of L+ in the reactor, thus suppressing L+ from being decomposed into L- and G. Period 2 was also related to the increase in velocity (0.03–0.06m/s), which was caused by the rapid increase in R_{PW} (0.8–1.4kg/m^3/s) due to the thermal insulation at the pyrolysis chamber's bottom. Fig. 6f illustrates that the PW pyrolysis duration was 21150s. From the beginning of char ignition (t=2040s) to the end of smoldering (t=21150s), the cumulative L+, L-, and G yields increased from 0 to 41.8%, 18.1%, and 36.4%, respectively. Moreover, the input energy to the pyrolysis chamber was 2573kJ, of which 599kJ was utilized, resulting in an energy efficiency e_E of 23.3% in this scenario.

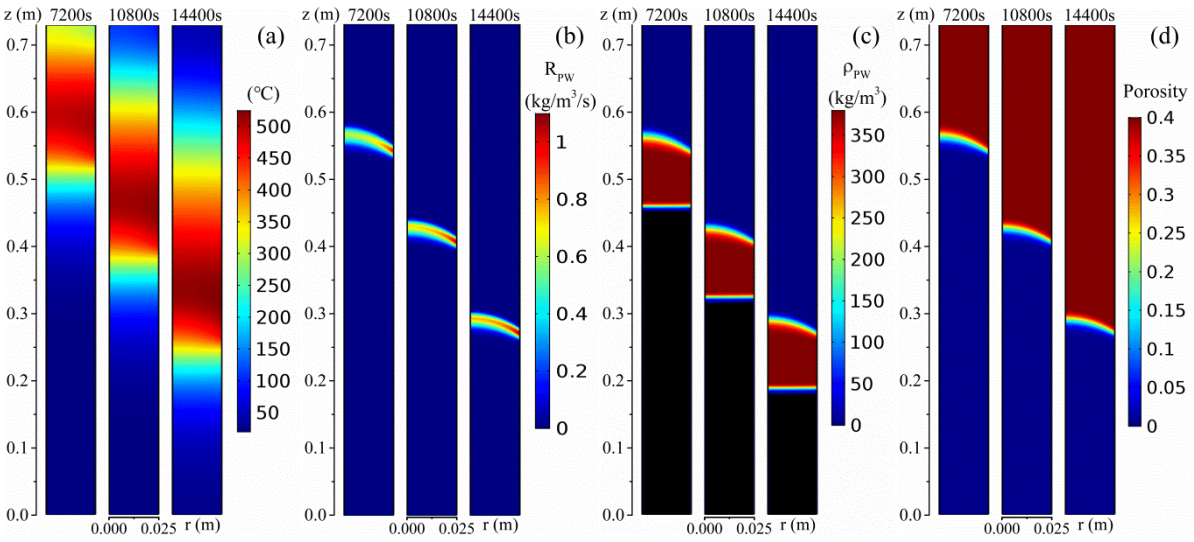

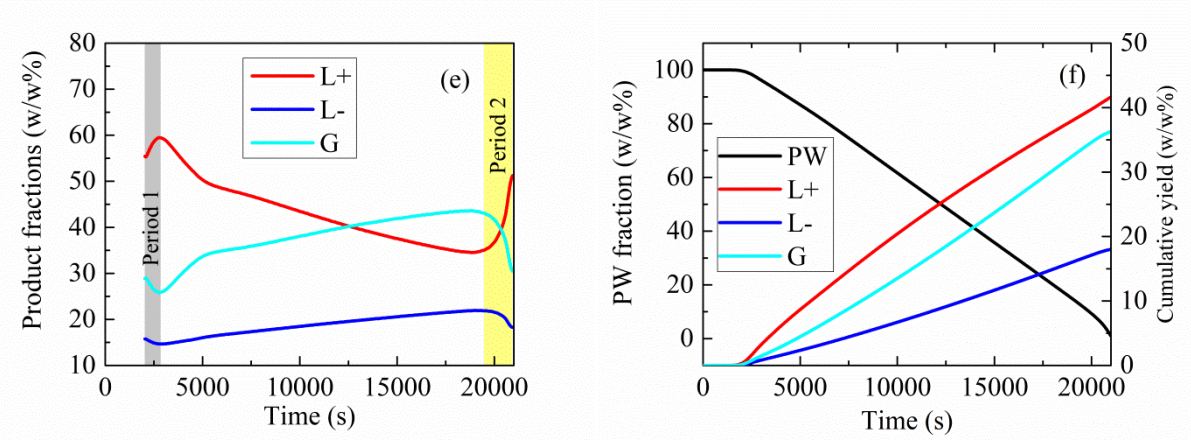

Fig. 6. Modelling results in PW pyrolysis chamber: (a) T_{PW}; (b) R_{PW}; (c) PW density; (d) Bed porosity; (e) Fractional distributions of pyrolysis products; (f) PW mass fraction and cumulative yields of products.

Fig. 7 shows the comparison of experimental and numerically calculated PW pyrolysis product yields and liquid fractions. The average peak value of T_{PW} was 510ºC (Fig. 5a). Maniscalco et al. [44] and López et al. [45] conducted the pyrolysis of PW at 500ºC. Fig. 7a illustrates that simulated liquid (L+ and L-) yield was slightly lower than the experimental one, and the simulated gas yield was higher than the experimental value. The difference could be attributed to the higher simulated temperature (510ºC) that decomposed the liquid into gas, resulting in a decrease in liquid yield and an increase in gas yield. Nonetheless, the numerically calculated product yields were close to the experimental results, with an error of 6.2%. Fig 7b shows that the numerically calculated L+ and L- fractions in liquid were in excellent agreement with the experimental results [33], with errors equaling 2.5% and 5.3%, respectively.

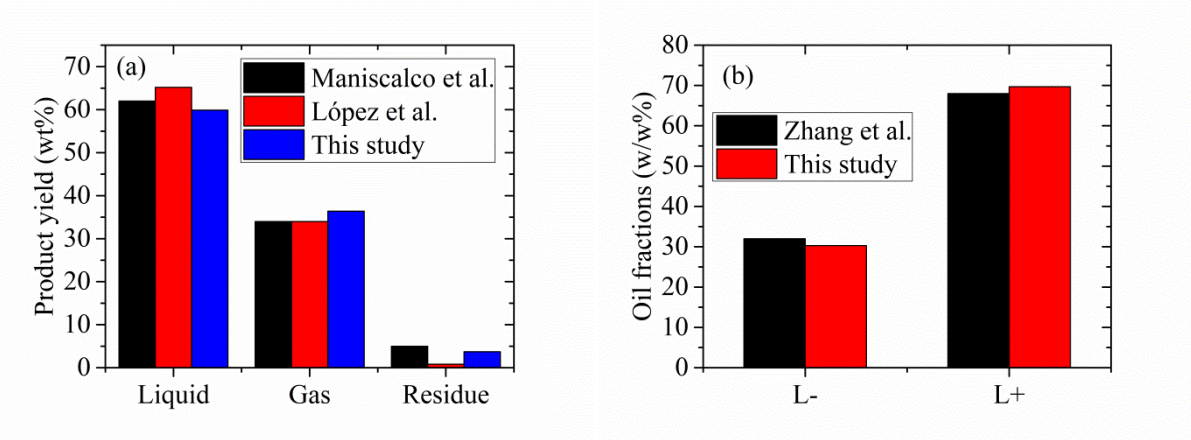

Fig. 7. Comparison of experimental and numerically calculated (a) product yields and (b) oil fractions.

3.3.Effect of char concentration

Fig. 8a demonstrates that the increase in char concentration could increase the peak value of T_{PW} (by 73℃) and shorten the pyrolysis duration (by 3780s). It is noteworthy that the local (smoldering front) energy balance in the smoldering chamber was determined by four parts: (i) energy generated from char oxidation; (ii) energy retained in the sand; (iii) energy transferred via conduction, convection, and radiation within the chamber; and (iv) out-of-chamber energy lost via conduction and convection. The out-of-chamber energy loss of smoldering could be divided into two parts: (i) the outward was lost to the environment, and (ii) the inward was utilized to heat the pyrolysis chamber. Higher char concentration could enhance the maximum char oxidation rate from 0.228min^{-1} to 0.310min^{-1}, increasing the local oxidation energy rate and further improving the local energy out rate [13]. Consequently, as the char concentration increased from 2.0% to 2.5%, the peak value of T_S increased from 620℃ to 678℃, and the smoldering propagation velocity increased from 2.25mm/min to 2.74mm/min. Considering the smoldering energy loss (ii), the peak value of T_{PW} was correspondingly increased, and the

pyrolysis duration was shortened. Moreover, Table 7 summarizes the quantitative expressions of char concentration effect on the peak value of T_{PW} and pyrolysis duration.

On the other hand, the random scissions of PW are more intense at higher temperatures, leading to a faster decomposition rate of PW [22]. The increase in char concentration led to an increment in R_{PW} (from 0.8kg/m^3/s to 1.4 kg/m^3/s) due to the higher T_{PW}. Accordingly, the velocity in the pyrolysis chamber increased from 0.030m/s to 0.036m/s due to the more intensive generation of volatiles (larger R_{PW}). Higher T_{PW} would affect the pyrolysis product yields in two ways: (i) exacerbating the L+ secondary cracking to decrease the L+ yield and increase the L- and G yields; and (ii) shortening the residence time of volatiles in the main reaction zone to prevent L+ from being decomposed into L- and G. Fig. 8b shows that the increase in char concentration would lead to a decrease in L- yield and an increase in G yield, indicating that (ii) was dominant in the L- yield and (i) determined the G yield. Moreover, the decrease in L+ yield revealed that (i) played a leading role in the L+ production. Table 7 lists the quantitative expressions of char concentration effect on the L+, L-, and G yields.

Fig. 8c demonstrates that higher char concentrations could input more energy into the pyrolysis chamber, which is not surprising since char oxidation released more heat as its concentration increased. The increment in char concentration led to a decrease in energy efficiency due to the excessive energy input. In other words, lower char concentrations could enhance the energy efficiency of the PW pyrolysis.

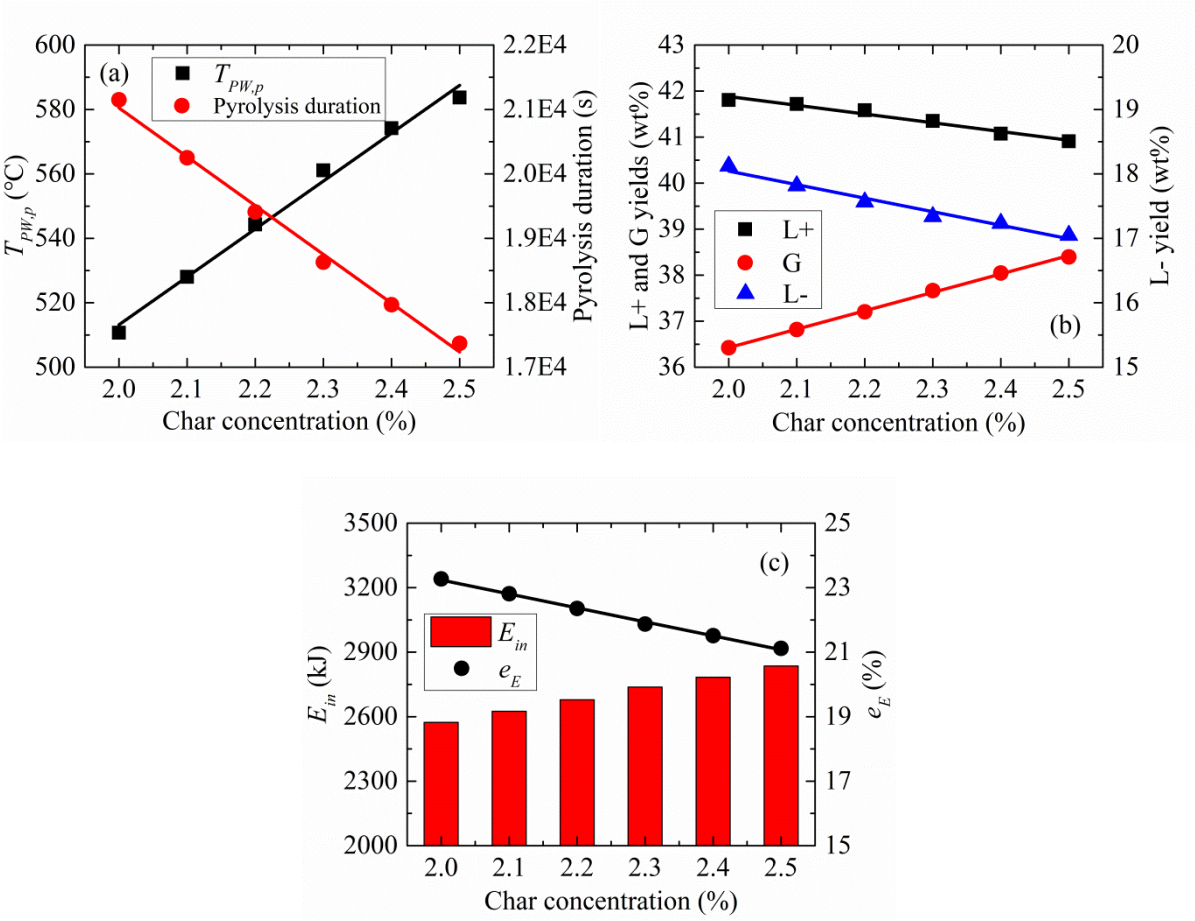

Fig. 8. Effect of char concentration on (a) $T_{PW,p}$ and pyrolysis duration, (b) product yields, and (c) input energy and energy efficiency.

Table 7. Quantitative expressions of char concentration effect.

Eq.	Expression	R^2 value
(39)	$T_{PW,p} = 148.64 \times C_{Char} + 215.88$	0.9908
(40)	$t = -7577.1 \times C_{Char} + 36179$	0.9942
(41)	$L+ = -1.8999 \times C_{Char} + 45.681$	0.9727
(42)	$L- = -2.1008 \times C_{Char} + 22.245$	0.9751
(43)	$G = 4.0007 \times C_{Char} + 28.424$	0.9989
(44)	$e_E = -4.3255 \times C_{Char} + 0.3189$	0.9976

3.4.Effect of air inlet velocity

The air inlet velocity is a crucial operating condition in the self-sustaining smoldering

process, which can regulate the oxygen supply [9]. As the air inlet velocity increased from 0.030m/s to 0.050m/s, the local consumed oxygen fraction decreased from 0.062 (0.204–0.142) to 0.052 (0.204–0.152). Due to the higher local oxygen fraction, the maximum char oxidation rate, determined by Eq. (2) , increased from 0.310min^{-1} to 0.380min^{-1}, leading to an increment in the local oxidation energy rate and further increased T_S (678–710ºC). The local energy out rate increased at faster air inlet velocities, which was attributed to the enhanced forward convection (caused by higher u_g) and conduction and radiation (caused by higher T_S) [4]. Consequently, the smoldering propagation velocity increased from 2.74mm/min to 3.92mm/min. As previously mentioned, the peak value of T_{PW} was correspondingly increased by 35ºC, and the pyrolysis duration was dramatically shortened by 3780s when the air inlet velocity increased from 0.030m/s to 0.050m/s (Fig. 9a). The specific expressions of char concentration effect on the peak value of T_{PW} and pyrolysis duration are tabulated in Table 8.

The increase in the T_{PW} peak led to an increment in the maximum R_{PW} (from 1.4kg/m^3/s to 2.0kg/m^3/s) due to the exacerbating random scissions of C–C bonds in PW [34]. On the other hand, the faster propagation velocity also resulted in more decomposition of PW in unit time. Combining the previous two influencing factors, the velocity in the pyrolysis chamber increased significantly from 0.036m/s to 0.076m/s by increasing the air inlet velocity over the studied range. Fig. 9b shows that the L+ was increased, and the L- and G yields were decreased at higher air inlet velocities, indicating that the suppression of L+ secondary cracking dominated the interconversion of volatiles (L+, L-, and G). Table 8 tabulates the quantitative expressions of air inlet velocity effect on the L+, L-, and G yields.

Fig. 9c demonstrates that increasing the air inlet velocity would reduce the input energy to the pyrolysis chamber, which was due to energy conservation as more energy was stored in the smoldering chamber [4]. Nevertheless, the input energy was sufficient to pyrolyze PW completely, i.e., the consumed energy remained unchanged, resulting in improved energy efficiency at higher air inlet velocities.

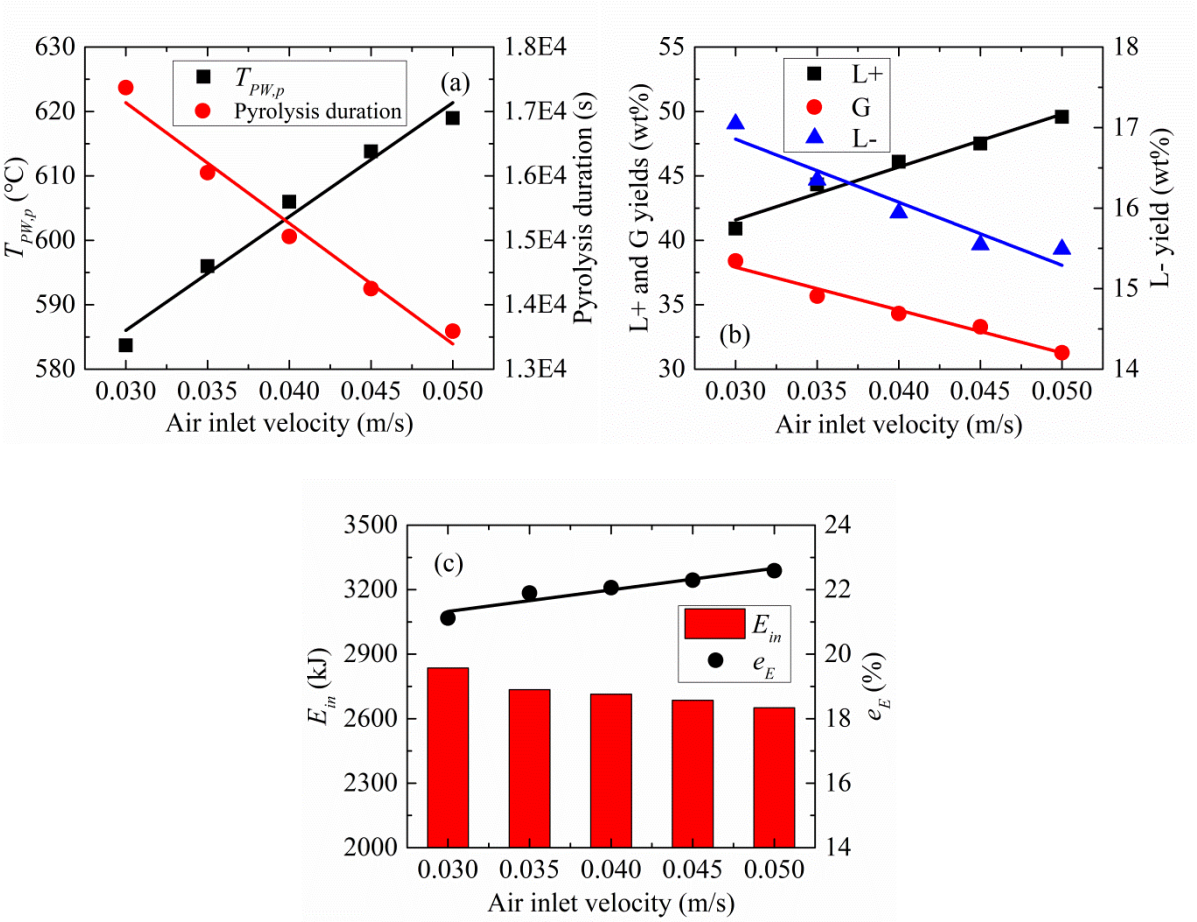

Fig. 9. Effect of air inlet velocity on (a) $T_{PW,p}$ and pyrolysis duration, (b) product yields, and (c) input energy and energy efficiency.

Table 8. Quantitative expressions of air inlet velocity effect.

Eq.	Expression	R^2 value
(45)	$T_{PW,p} = 1767.1 \times u_{g,in} + 533.01$	0.9760

(46)	$t = -187200 \times u_{g,in} + 22752$	0.9816
(47)	$L+ = 410.56 \times u_{g,in} + 29.264$	0.9722
(48)	$L- = -78.312 \times u_{g,in} + 19.206$	0.9243
(49)	$G = -332.25 \times u_{g,in} + 47.880$	0.9724
(50)	$e_E = 0.6683 \times u_{g,in} + 0.1932$	0.9104

3.5.Effect of PW content

The initial mass of the reactants will change the heat and mass transfer within the reactor, thereby affecting the pyrolysis process [46]. Fig. 10a demonstrates that the peak T_{PW} hovered around 580℃ (±1.4℃) in the range of PW content studied, which indicated that the PW content had little effect on the temperature distribution in the pyrolysis chamber. Moreover, as the PW content increased from 0.30 to 0.50, the pyrolysis duration was slightly prolonged by 240s, which could be ascribed to the more energy consumed by PW pyrolysis slowing down the propagation velocity.

Even though T_{PW} remained almost unchanged at higher PW contents, the initial PW bulk density increased by a factor of 1.67 (285–475kg/m^3), which caused R_{PW} (determined by Eq. 6) to increase from 1.1kg/m^3/s to 1.6 kg/m^3/s. The residence time of volatiles dominated the inter-transformation of volatiles due to the almost unchanged T_{PW} at different PW contents. The production of more intensive volatiles resulted in an increment in the velocity within the pyrolysis chamber from 0.028m/s to 0.045m/s. In other words, the residence time of volatiles in the main reaction zone was shortened, further inhibiting the decomposition of L+ into L- and G. Therefore, as depicted in Fig. 10b, the increase in PW content led to an increase in L+ yield (36.3–44.10wt%) and a decrease in L- (17.8–16.6wt%) and G (42.2–35.7wt%) yields. Table 9 lists the specific expressions of PW content's effect on the yields of PW pyrolysis

volatiles.

Fig. 10c shows that the increase in PW content led to an increment in input energy from 2667kJ to 3057kJ. The increasing PW content reduced the effective thermal conductivity (Eq. 37) and slowed down the overall heating rate of the pyrolysis chamber, resulting in more energy input from the boundary. On the other hand, the consumed energy increased from 449kJ to 749kJ by increasing PW content over the studied range, which led to an increase in energy efficiency from 16.84% to 24.84%.

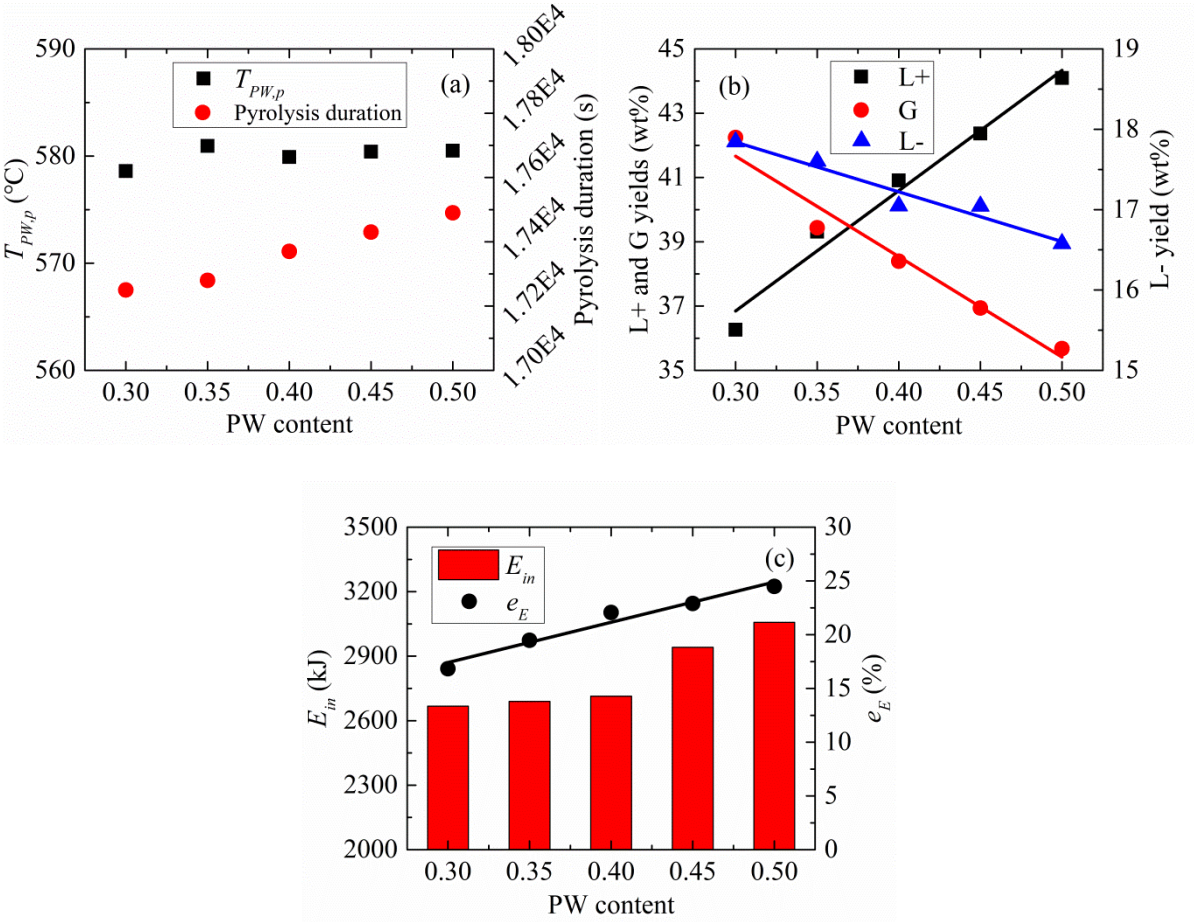

Fig. 10. Effect of PW content on (a) $T_{PW,p}$ and pyrolysis duration, (b) product yields, and (c) input energy and energy efficiency.

Table 9. Quantitative expressions of PW content's effect.

Eq.	Expression	R^2 value
(51)	$L+ = 37.443 \times C_{PW} + 25.613$	0.9760
(52)	$L- = -6.1865 \times C_{PW} + 19.696$	0.9468
(53)	$G = -31.257 \times C_{PW} + 51.041$	0.9655
(54)	$e_E = 0.3744 \times C_{PW} + 0.0618$	0.9621

4. Conclusions

This study proposed a novel smoldering-driven reactor for the pyrolysis of plastic waste (PW). The reactor consisted of two chambers: the smoldering chamber for char smoldering to provide heat, and the pyrolysis chamber for PW pyrolysis using the smoldering heat. A multidimensional model was developed to verify the feasibility of the reactor and evaluate its performance. To the best of our knowledge, it was the first effort for a numerical investigation of smoldering-driven PW pyrolysis, including the melting process. The findings revealed that char concentration, air inlet velocity, and PW content affected the PW pyrolysis duration, product yields, and energy efficiency. The following summarized the main achievements and conclusions of this study.

The char smoldering could self-sustainingly propagate with a steady propagation velocity and temperature in the sand-filled smoldering chamber, indicating that this reactor could also treat organic-contaminated sand. The porous matrix could address the uneven radial temperature distribution in the pyrolysis chamber due to the low thermal conductivity of PW.

The increment in char concentration could improve the propagation velocity and peak temperature. The increased propagation velocity shortened the PW pyrolysis duration by approximately one hour. The increase in peak temperature led to a decrease in light liquid (L-,

C5–C15) and heavy liquid (L+, >C15) yields and an increase in gas (G, C1–C4) yield. Lower char concentrations could enhance the energy efficiency of the PW pyrolysis by 2.15%.

Increasing the air inlet velocity shortened the PW pyrolysis duration by 3780s. Higher air inlet velocities favored the L+ production but were not conducive to the L- and G production. The energy efficiency could be enhanced by 1.47% by increasing the air inlet velocity over the studied range.

Higher PW contents increased the velocity in the pyrolysis chamber, resulting in an increase in L+ yield and a decrease in L- and G yields. Increasing the PW content (0.30–0.50) led to a significant increase in the energy efficiency from 16.84% to 24.84%.

Acknowledgements

This work was supported by the China Scholarship Council (CSC) program (No. 201906120036). The authors appreciate Dr. Z. Till for providing the plastic pyrolysis kinetic parameters. Thanks are given to Dr. M.A.B. Zanoni for providing the smoldering experimental data and having valuable discussions.

Conflict of interest

The authors declare no competing financial interest.

References

[1] Torero, J.L., Gerhard, J.I., Martins, M.F., Zanoni, M.A., Rashwan, T.L. and Brown, J.K., 2020. Processes defining smouldering combustion: Integrated review and synthesis. Progress in Energy and Combustion Science, 81, p.100869. https://doi.org/10.1016/j.pecs.2020.100869

[2] Song, Z., Huang, X., Kuenzer, C., Zhu, H., Jiang, J., Pan, X. and Zhong, X., 2020. Chimney effect induced by smoldering fire in a U-shaped porous channel: A governing mechanism of the persistent underground coal fires. Process Safety and Environmental Protection, 136, pp.136-147. https://doi.org/10.1016/j.psep.2020.01.029

[3] Miry, S., Gerhard, J., Zanoni, M. and Rashwan, T., 2021. Validation of a Multidimensional Smouldering Model. https://doi.org/10.1002/essoar.10508380.1

[4] Zanoni, M.A., Torero, J.L. and Gerhard, J.I., 2019. Delineating and explaining the limits of self-sustained smouldering combustion. Combustion and Flame, 201, pp.78-92. https://doi.org/10.1016/j.combustflame.2018.12.004

[5] Pironi, P., Switzer, C., Rein, G., Fuentes, A., Gerhard, J.I. and Torero, J.L., 2009. Small-scale forward smouldering experiments for remediation of coal tar in inert media. Proceedings of the Combustion Institute, 32(2), pp.1957-1964. https://doi.org/10.1016/j.proci.2008.06.184

[6] Rashwan, T.L., Gerhard, J.I. and Grant, G.P., 2016. Application of self-sustaining smouldering combustion for the destruction of wastewater biosolids. Waste management, 50, pp.201-212. https://doi.org/10.1016/j.wasman.2016.01.037

[7] Yermán, L., Hadden, R.M., Carrascal, J., Fabris, I., Cormier, D., Torero, J.L., Gerhard, J.I., Krajcovic, M., Pironi, P. and Cheng, Y.L., 2015. Smouldering combustion as a treatment technology for faeces: exploring the parameter space. Fuel, 147, pp.108-116. https://doi.org/10.1016/j.fuel.2015.01.055

[8] Vantelon, J.P., Lodeho, B., Pignoux, S., Ellzey, J.L. and Torero, J.L., 2005. Experimental observations on the thermal degradation of a porous bed of tires. Proceedings of the Combustion Institute, 30(2), pp.2239-2246. https://doi.org/10.1016/j.proci.2004.08.109

[9] Song, Z., He, T., Li, M., Wu, D. and You, F., 2022. Self-sustaining smoldering as a novel disposal approach for food waste with high moisture content. Fuel Processing Technology, 228, p.107144. https://doi.org/10.1016/j.fuproc.2021.107144

[10] Rashwan, T.L., Fournie, T., Torero, J.L., Grant, G.P. and Gerhard, J.I., 2021. Scaling up self-sustained smouldering of sewage sludge for waste-to-energy. Waste Management, 135, pp.298-308. https://doi.org/10.1016/j.wasman.2021.09.004

[11] Xia, T.X., Greaves, M., Turta, A.T. and Ayasse, C., 2003. THAI—A 'short-distance displacement'in situ combustion process for the recovery and upgrading of heavy oil. Chemical Engineering Research and Design, 81(3), pp.295-304. https://doi.org/10.1205/02638760360596847

[12] Duque, J.V.F., Bittencourt, F.L., Martins, M.F. and Debenest, G., 2021. Developing a combustion-driven reactor for waste conversion. Energy, 237, p.121489. https://doi.org/10.1016/j.energy.2021.121489

[13] Duque, J.V.F., Martins, M.F., Bittencourt, F.L. and Debenest, G., 2021. Relevant aspects

of propagating a combustion front in an annular reactor for out-of-bed heat recovery. Experimental Thermal and Fluid Science, p.110575. https://doi.org/10.1016/j.expthermflusci.2021.110575

[14] Debenest, G., Guibert, R., Horgue, P. and Yang, C., 2020. Numerical Simulation of Solid Combustion in Microporous Particles. Frontiers in Chemistry, 8. https://doi.org/10.3389/fchem.2020.510686

[15] Bittencourt, F.L.F., Martins, M.F., Orlando, M.T.D. and Galvão, E.S., 2022. The proof-of-concept of a novel feces destroyer latrine. Journal of Environmental Chemical Engineering, 10(1), p.106827. https://doi.org/10.1016/j.jece.2021.106827

[16] Ronda, A., Della Zassa, M., Biasin, A., Martin-Lara, M.A. and Canu, P., 2017. Experimental investigation on the smouldering of pine bark. Fuel, 193, pp.81-94. https://doi.org/10.1016/j.fuel.2016.12.028

[17] Feng, C., Huang, J., Yang, C., Li, C., Luo, X., Gao, X. and Qiao, Y., 2021. Smouldering combustion of sewage sludge: Volumetric scale-up, product characterization, and economic analysis. Fuel, 305, p.121485. https://doi.org/10.1016/j.fuel.2021.121485

[18] He, F., Yi, W., Li, Y., Zha, J. and Luo, B., 2014. Effects of fuel properties on the natural downward smoldering of piled biomass powder: Experimental investigation. Biomass and Bioenergy, 67, pp.288-296. https://doi.org/10.1016/j.biombioe.2014.05.003

[19] Bittencourt, F.L.F., Debenest, G. and Martins, M.F., 2022. Free convection development caused by bed shrinkage in a vacuum-induced smoldering reactor. Chemical Engineering Journal, 430, p.132847. https://doi.org/10.1016/j.cej.2021.132847

[20] Zanoni, M.A., Wang, J. and Gerhard, J.I., 2021. Understanding pressure changes in smouldering thermal porous media reactors. Chemical Engineering Journal, 412, p.128642. https://doi.org/10.1016/j.cej.2021.128642

[21] Jie, X., Li, W., Slocombe, D., Gao, Y., Banerjee, I., Gonzalez-Cortes, S., Yao, B., AlMegren, H., Alshihri, S., Dilworth, J. and Thomas, J., 2020. Microwave-initiated catalytic deconstruction of plastic waste into hydrogen and high-value carbons. Nature Catalysis, 3(11), pp.902-912. https://doi.org/10.1038/s41929-020-00518-5

[22] Wang, C., Zou, R., Lei, H., Qian, M., Lin, X., Mateo, W., Wang, L., Zhang, X. and Ruan, R., 2021. Biochar-advanced thermocatalytic salvaging of the waste disposable mask with the production of hydrogen and mono-aromatic hydrocarbons. Journal of Hazardous Materials, p.128080. https://doi.org/10.1016/j.jhazmat.2021.128080

[23] Mazloum, S., Aboumsallem, Y., Awad, S., Allam, N. and Loubar, K., 2021. Modelling pyrolysis process for PP and HDPE inside thermogravimetric analyzer coupled with differential scanning calorimeter. International Journal of Heat and Mass Transfer, 176, p.121468. https://doi.org/10.1016/j.ijheatmasstransfer.2021.121468

[24] Yin, L.J., Chen, D.Z., Wang, H., Ma, X.B. and Zhou, G.M., 2014. Simulation of an innovative reactor for waste plastics pyrolysis. Chemical Engineering Journal, 237, pp.229-235. https://doi.org/10.1016/j.cej.2013.09.114

[25] Mazloum, S., Awad, S., Allam, N., Aboumsallem, Y., Loubar, K. and Tazerout, M., 2021. Modelling plastic heating and melting in a semi-batch pyrolysis reactor. Applied Energy, 283, p.116375. https://doi.org/10.1016/j.apenergy.2020.116375

[26] Ding, K., Xiong, Q., Zhong, Z., Zhong, D. and Zhang, Y., 2020. CFD simulation of combustible solid waste pyrolysis in a fluidized bed reactor. Powder Technology, 362, pp.177-187. https://doi.org/10.1016/j.powtec.2019.12.011

[27] Murata, K., Sakata, Y. and Brebu, M., 2022. Thermal degradation of polyethylene in the presence of a non-acidic porous solid by a continuous flow reactor. Journal of Analytical and Applied Pyrolysis, 161, p.105395. https://doi.org/10.1016/j.jaap.2021.105395

[28] Shi, X., Zhang, Y., Chen, X. and Zhang, Y., 2021. Effects of thermal boundary conditions on spontaneous combustion of coal under temperature-programmed conditions. Fuel, 295, p.120591. https://doi.org/10.1016/j.fuel.2021.120591

[29] Shi, X., Zhang, Y., Chen, X., Zhang, Y. and Ma, T., 2021. Numerical study on the oxidation reaction characteristics of coal under temperature-programmed conditions. Fuel Processing Technology, 213, p.106671. https://doi.org/10.1016/j.fuproc.2020.106671

[30] Till, Z., Varga, T., Sója, J., Miskolczi, N. and Chován, T., 2018. Kinetic identification of plastic waste pyrolysis on zeolite-based catalysts. Energy Conversion and Management, 173, pp.320-330. https://doi.org/10.1016/j.enconman.2018.07.088

[31] Till, Z., Varga, T., Sója, J., Miskolczi, N. and Chován, T., 2020. Structural assessment of lumped reaction networks with correlating parameters. Energy Conversion and Management, 209, p.112632. https://doi.org/10.1016/j.enconman.2020.112632

[32] Ceamanos, J., Mastral, J.F., Millera, A. and Aldea, M.E., 2002. Kinetics of pyrolysis of high density polyethylene. Comparison of isothermal and dynamic experiments. Journal of Analytical and Applied Pyrolysis, 65(2), pp.93-110.

https://doi.org/10.1016/S0165-2370(01)00183-8

[33] Zhang, Y., Fu, Z., Wang, W., Ji, G., Zhao, M. and Li, A., 2021. Kinetics, Product Evolution, and Mechanism for the Pyrolysis of Typical Plastic Waste. ACS Sustainable Chemistry & Engineering. https://doi.org/10.1021/acssuschemeng.1c04915

[34] Pan, R., Martins, M.F. and Debenest, G., 2021. Pyrolysis of waste polyethylene in a semi-batch reactor to produce liquid fuel: Optimization of operating conditions. Energy Conversion and Management, 237, p.114114. https://doi.org/10.1016/j.enconman.2021.114114

[35] Shi, X., Zhang, Y., Chen, X., Zhang, Y., Rui, L., Guo, R., Zhao, T. and Deng, Y., 2022. Numerical simulation on response characteristics of coal ignition under the disturbance of fluctuating heat. Combustion and Flame, 237, p.111870. https://doi.org/10.1016/j.combustflame.2021.111870

[36] Zanoni, M.A., Torero, J.L. and Gerhard, J.I., 2017. Determination of the interfacial heat transfer coefficient between forced air and sand at Reynold's numbers relevant to smouldering combustion. International Journal of Heat and Mass Transfer, 114, pp.90-104. https://doi.org/10.1016/j.ijheatmasstransfer.2017.06.020

[37] Lougou, B.G., Han, D., Zhang, H., Jiang, B., Anees, J., Ahouannou, C., Zhao, J. and Shuai, Y., 2020. Numerical and experimental analysis of reactor optimum design and solar thermal-chemical energy conversion for multidisciplinary applications. Energy Conversion and Management, 213, p.112870. https://doi.org/10.1016/j.enconman.2020.112870

[38] Zhang, J. and Liu, Z., 2006. A study on the convective heat transfer coefficient of concrete in wind tunnel experiment. China Civil Engineering Journal, 9. DOI: 10.3321j.issn1000-131X.2006.09.006.

[39] Mamalis, A.G., Spentzas, K.N., Kouzilos, G., Theodorakopoulos, I. and Pantelelis, N.G., 2010. On the high‐density polyethylene extrusion: Numerical, analytical and experimental modeling. Advances in Polymer Technology, 29(3), pp.173-184. https://doi.org/10.1002/adv.20185

[40] Agassant, J.F., Pigeonneau, F., Sardo, L. and Vincent, M., 2019. Flow analysis of the polymer spreading during extrusion additive manufacturing. Additive Manufacturing, 29, p.100794. https://doi.org/10.1016/j.addma.2019.100794

[41] Wong, A.Y. and Liang, J.Z., 1994. Temperature and pressure effects on the melt index and melt density of high-density polyethylene. Journal of materials processing technology, 43(2-4), pp.293-304. https://doi.org/10.1016/0924-0136(94)90027-2

[42] Shi, X., Zhang, Y., Chen, X., Zhang, Y. and Ma, Q., 2021. Characteristics of coal dust ignited by a hot particle. Process Safety and Environmental Protection, 153, pp.225-238. https://doi.org/10.1016/j.psep.2021.07.021

[43] Shi, X., Chen, X., Zhang, Y., Zhang, Y., Guo, R., Zhao, T. and Liu, R., 2022. Numerical simulation of coal dust self–ignition and combustion under inclination conditions. Energy, 239, p.122227. https://doi.org/10.1016/j.energy.2021.122227

[44] Maniscalco, M., La Paglia, F., Iannotta, P., Caputo, G., Scargiali, F., Grisafi, F. and Brucato, A., 2021. Slow pyrolysis of an LDPE/PP mixture: Kinetics and process

performance. Journal of the Energy Institute, 96, pp.234-241. https://doi.org/10.1016/j.joei.2021.03.006

[45] Lopez, A., De Marco, I., Caballero, B.M., Laresgoiti, M.F. and Adrados, A., 2011. Influence of time and temperature on pyrolysis of plastic wastes in a semi-batch reactor. Chemical Engineering Journal, 173(1), pp.62-71. https://doi.org/10.1016/j.cej.2011.07.037

[46] Yamada, H., Kiatkittipong, W. and Tagawa, T., 2022. Catalyst screening for heavy oil production from waste plastic. Environmental Challenges, p.100444. https://doi.org/10.1016/j.envc.2022.100444